Journal of Alloys and Compounds 1010 (2025) 177102

Contents lists available at ScienceDirect

Journal of Alloys and Compounds

journal homepage: www.elsevier.com/locate/jalcom

# A novel approach to enhancing performance and endurance in $GeS_2$ OTS devices using amorphous carbon doped $W_2N$ electrodes

Minkyu Lee [a], Sanghyeon Lee [a], Myoungsub Kim [b], Jinhan Lee [a], Chaebeen Kwon [a], Chihyeong Won [a], Seungmin Lee [a], Sungjoon Cho [a], Seunggyu Na [a], Jongho Ji [a], Hanjoo Lee [a], Kukro Yoon [a], Hyun S. Kum [a], Hyungjun Kim [a], Taeyoon Lee [a,*]

[a] School of Electrical and Electronic Engineering, Yonsei University, Seoul 03722, Republic of Korea
[b] SK hynix Inc, 2091, Gyeongchung-daero, Bubal-eup, Icheon-si, Gyeonggi-do, Republic of Korea

ARTICLE INFO

*Keywords:*
Tungsten Nitride
Amorphous carbon
Germanium Sulfide
OTS selector
Cross–point memory

ABSTRACT

Three–dimensional (3D) cross-point (X–point) memory has gathered interest for its fast data processing and high density, achieved by stacking memory with a selector device to prevent misinterpretation. Ovonic threshold switching (OTS) is a promising selector due to its reversible switching behavior. Although, OTS devices typically employ transition metal nitrides (TMN) such as $TiN_x$, $TaN_x$, and $WN_x$ for electrodes owing to their good stability, high melting points, and low resistivity, TMNs can diffuse and degrade device performance by recrystallizing with chalcogenide alloys. Amorphous carbon (a–C) can be a good alternative electrode material due to its low roughness, cost–effectiveness, high work function (WF), and excellent thermal stability. However, the high resistivity of a–C (~ 150 mΩ–cm) increases threshold voltage ($V_{th}$), causing high power consumption. Therefore, combining both a–C and TMN materials can effectively obtain their advantages. This study explores the effect of varying a–C content in $W_2N$ electrodes on $GeS_2$–based OTS selectors. The $(W_2N)_{1-x}C_x$ ($0 \le x \le 0.25$) electrodes were deposited using DC magnetron co–sputtering. The phase of $(W_2N)_{1-x}C_x$ ($0 \le x \le 0.25$) films transformed from polycrystalline to amorphous with increasing x. Devices with $(W_2N)_{1-x}C_x/GeS_2/W_2N$ structure showed decreased $V_{th}$ and off current, improving from 4.8 to 3.8 V and 8.0–4.17 nA, respectively. The subthreshold slope, distance between traps, and interface trap density ($N_{it}$) were extracted using the Pool–Frenkel model. The reduced $V_{th}$ may be attributed to a higher WF and lower $N_{it}$ with increasing x. The device's lifetime improved up to $1.0 \times 10^9$ pulses for the highest a–C content in $(W_2N)_{1-x}C_x$ ($0 \le x \le 0.25$) electrodes.

## 1. Introduction

Three–dimensional (3D) cross–point (X–point) memory has attracted interest for its advantage on fast data processing time and high density [1–4]. This structure is constructed by stacking memory with selector devices to prevent misinterpretation [5,6]. Ovonic threshold switching (OTS) can be the most suitable candidate for selector devices due to its reversible electrical switching behavior [7,8]. An OTS device is fabricated by depositing electrodes between chalcogenide alloys. In addition, transition metal nitrides (TMN) such as $TiN_x$, $TaN_x$, and $WN_x$ are widely used electrodes because of their desirable properties such as physical/chemical inertness, high melting temperature, and low resistivity [9–12]. However, diffusion of transition metals recrystallizes with chalcogenide alloys, degrading the device [13]. Ding *et al.* fabricated a single–element Te selector using TiN as the top electrode, which showed a low threshold voltage ($V_{th}$, 1.3 V), selectivity of $10^3$, and thermal stability up to 430 °C. After $10^9$ cycles of AC pulses, the device degraded due to Ti diffusion into Te and crystallized to TiTe [14]. In addition, deposited TMNs are usually grown in polycrystalline, increasing roughness and causing more inactive contacts [15–17].

Amorphous carbon (a–C), conductive material, is an appealing electrode due to its low roughness, cost–effectiveness, high work function (WF, 5.11 eV), and high thermal stability [18–20]. Verdy *et al.* fabricated TiN/carbon electrode for a Ge–Se–Sb based OTS selector. This electrode enhanced lifetime of the device by preventing the crystallization of chalcogenide alloys even after $10^9$ pulses [21]. However, the high resistivity of a–C (~ 150 mΩ–cm) increases $V_{th}$, causing power consumption [22]. One of the effective methods to attain both the

* Corresponding author.
*E-mail address:* taeyoon.lee@yonsei.ac.kr (T. Lee).

https://doi.org/10.1016/j.jallcom.2024.177102
Received 24 June 2024; Received in revised form 10 October 2024; Accepted 16 October 2024
Available online 17 October 2024
0925-8388/© 2024 Published by Elsevier B.V.

advantages of TMNs and a–C can be incorporating a–C into TMN.

Here, we demonstrate the influence of varying a–C contents in the $W_2N$ electrodes and its effect on the $GeS_2$–based OTS selector device. The $(W_2N)_{1\text{-}x}C_x$ ($0 \leq x \leq 0.25$) electrodes are deposited using DC magnetron co–sputtering to investigate their microstructure, electrical properties, and device characteristics. According to the x–ray diffraction (XRD) and high–resolution transmission electron microscopy (HRTEM) analyses, the phases of $(W_2N)_{1\text{-}x}C_x$ electrodes transformed from polycrystalline to amorphous as the content of a–C increased. The roughness of $(W_2N)_{1\text{-}x}C_x$ electrodes also decreased because the film became more amorphous–like phase, which gradually decreased grain size. The resistivity of $(W_2N)_{1\text{-}x}C_x$ was measured using a four–point probe method with the range of 0.211 – 1.940 mΩ–cm. To study the electrical characteristics of $(W_2N)_{1\text{-}x}C_x$ electrodes, devices were fabricated with $(W_2N)_{1\text{-}x}C_x/GeS_2/W_2N$ structure. $GeS_2$ is the most suitable candidate due to its high thermal stability (~ 600 °C) compared to Ge–Se (400 ~ 450 °C) and Ge–Te (200 ~ 260 °C), which allows for high–temperature processing and does not require additional process such as doping or incorporating other materials [23–25]. In DC–IV characteristics, both $V_{th}$ and off current ($I_{off}$) of selector devices decreased from 4.8 to 3.8 V and 8.0–4.17 nA, respectively, as increasing a–C composition. According to Pool–Frenkel model, the subthreshold slope (*STS*) and distance between traps ($\Delta z$) increased from 1.15 to 1.35 V/dec and 0.89–1.05 nm, respectively. Interface trap density ($N_{it}$), which is inversely proportional to $\Delta z$, decreased from $14.35 \times 10^{20}$ to $8.76 \times 10^{20}$ cm$^{-3}$. The decreased $V_{th}$ may be attributed to increased WF and decreased $N_{it}$ with increasing a–C composition. In transient responses, the lifetime of selector devices increased from $5.0 \times 10^7$ to $1.0 \times 10^9$ pulses.

## 2. Material and methods

### 2.1. Sample preparation

DC magnetron sputtering (SNTEK Co., LTD) was employed to deposit $(W_2N)_{1\text{-}x}C_x$ films using W and a–C targets, purchased from AVENTION (2–inch diameter, 3–mm thick) and PRAXAIR (2–inch diameter, 3–mm thick). Under a base pressure lower than 6E$^{-6}$ Torr, $Ar/N_2$ gas with a flow ratio of 20/7 sccm was injected at a working pressure of 4 mTorr. The plasma power for W target was fixed at 150 W. To investigate broad compositions of a–C, plasma power for a–C target was increased from 0 to 70 W. The $GeS_2$ film was deposited using RF magnetron sputtering. Under same base pressure, Ar gas flow of 15 sccm was injected with working pressure of 3 mTorr. The plasma power was fixed at 50 W. A 300–nm–thick $SiO_2$/Si($P^+$) wafer was used as the substrate.

### 2.2. Film analysis

The thickness of the deposited films was measured using field emission scanning electron microscopy (JSM–7610–Plus) and HRTEM (Thermo Fisher Scientific, Thermis Z). The quantitative ratios of W, N, and C were confirmed using auger electron spectroscopy (AES, ULVAC, PHI–710) and X–ray photoelectron spectroscopy (XPS, XPS_UPS, Nexsa). The film densities were calculated by employing X–ray reflectance (XRR, Rigaku, SmartLab). To measure roughness, noncontact–mode atomic force microscopy (NC–AFM, Park Systems, NX–10) was employed. The crystal planes of films were confirmed through XRD (Rigaku, SmartLab) and HRTEM.

### 2.3. Electrical measurements

To measure electrical characteristics, a Keithley 4200A–SCS semiconductor parameter analyzer was employed. Using four–point probe set–up, resistivity of each film was measured. In case of device characteristics, a 100–nm–thick $W_2N$ bottom electrode was deposited by DC magnetron sputtering on glass substrate. Then, $GeS_2$ selector layer was deposited on top of the bottom electrode and shadow mask. Then, patterned 50–μm–diameter $(W_2N)_{1\text{-}x}C_x$ top electrode was deposited with thickness of 30 nm. The transient characteristics were measured using external phase measurement unit sensors

## 3. Results and discussion

### 3.1. Growth of tungsten nitride carbide films

Fig. 1a illustrates the DC magnetron co-sputtering deposition system. The $(W_2N)_{1\text{-}x}C_x$ ($0 \leq x \leq 0.25$) films were deposited using W and a–C targets. To modulate various compositions, the a–C target power was varied from 0 to 70 W with a fixed W target power of 150 W. Both the AES was employed to quantify a–C content in $(W_2N)_{1\text{-}x}C_x$ films with increasing applied a–C target powers, of which contents are presented in Fig. 1b. With increasing C contents from 0 to 25.27 at%, W and N contents gradually decreased from 71.72 to 51.48 at% and 27.94–22.23 at%, respectively. The overall AES spectra were shown in Figure S1 a–f. Fig. 1c shows that the resistivity of $(W_2N)_{1\text{-}x}C_x$ films increased from 0.211 to 1.940 mΩ–cm with increasing x from 0 to 0.25. The elevated resistivity could be attributed to both the high resistivity of C and deformation of microstructure, which will be discussed in more detail in Fig. 2. Fig. 1d represents density variation with x of $(W_2N)_{1\text{-}x}C_x$ layers, which was extracted from XRR patterns. The density of $(W_2N)_{1\text{-}x}C_x$ films increased from 9.11 to 11.08 g/cm$^3$ with increasing x. Without incorporating C, the grown $W_2N$ films cannot avoid various voided regions in the microstructure due to inherent columnar porous structure caused by sputtering deposition. Once C was incorporated into films, small atomic size of C fills voided regions and hinders grain growth, resulting in higher density [26]. Fig. 1e shows the variation in roughness of $(W_2N)_{1\text{-}x}C_x$ films via NC–AFM measurements. The roughness of the $W_2N$ film was measured to be 2.31 nm. With increasing x to 0.25, the roughness gradually decreased up to 0.65 nm. With increasing C contents, C interrupts grain growths, which allows to attain smoother surfaces [27]. Fig. 1f presents representative surface morphology images obtained by AFM measurements at $x = 0$ and $x = 0.25$ of $(W_2N)_{1\text{-}x}C_x$ films, which coincide with the results of Fig. 1e.

### 3.2. Structural analysis

Fig. 2a demonstrates the XRD patterns of $(W_2N)_{1\text{-}x}C_x$ films grown on $SiO_2$ substrates with x ranging from 0 to 0.25. The XRD pattern of $W_2N$ film (gray color) initially presented multiple orientations of (111) and (200) crystal planes of the face–centered cubic (fcc) β–$W_2N$ structure (JCPDS card No. 01–075–1012) [28,29]. Once C was incorporated, relative peak intensities gradually decreased corresponding to the increasing contents of C. When the x of $(W_2N)_{1\text{-}x}C_x$ films increased up to 0.25, (200) peak almost disappeared. The preferential (111) peak was broadened, of which position lied intermediate between bulk $W_2C$ and $W_2N$ peaks. The magnified XRD patterns (top right side inset) showed that (111) β–$W_2N$ peaks continuously shifted toward to lower 2θ values of 35.96° with increasing x to 0.25. This shift can be attributed to the compressive stress induced by the change in film composition [30]. The average grain size of $(W_2N)_{1\text{-}x}C_x$ can be estimated using the Debey–-Scherrer equation as follows:

$$L \quad (average\ grain\ size) = \frac{k\lambda}{\mathrm{FWHM}\cos(\theta)}$$

where k is Scherrer constant, λ is X–ray wavelength (0.15418 for Cu K–alpha), FWHM is full width at half maximum, and θ is Bragg angle [31]. The FWHM was extracted from the first–order peak as shown in Figure S2a. The FWHM of $(W_2N)_{1\text{-}x}C_x$ films was found to be 0.62, 0.92, 0.98, 1.24, 1.74, and 2.60, respectively. Subsequently, the average grain size was estimated to be 14.15, 9.53, 8.95, 7.07, 5.04, and 3.37 nm, respectively with increasing contents of C as shown in Figure S2b. The average grain size, estimated to be 14.45 nm for the pure $W_2N$ film,

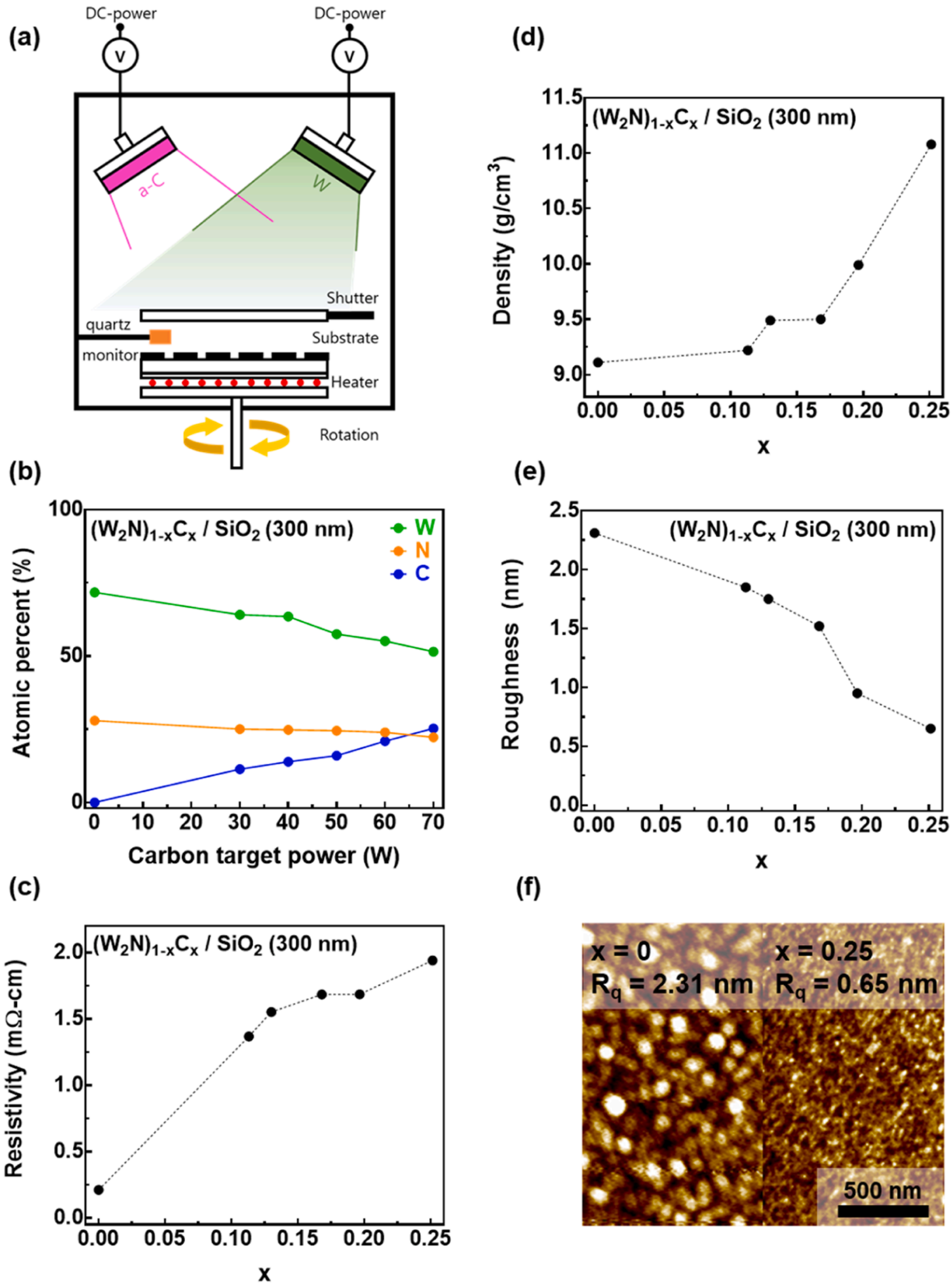


**Fig. 1.** (a) DC–DC sputtering set–up, (b) Summarized Auger Electron Spectroscopy (AES) of $(W_2N)_{1-x}C_x$ films. (c) Resistivity of $(W_2N)_{1-x}C_x$ films using four–point probe. (d) Calculated density from X–ray reflectivity (XRR). (e) Summarized roughness of $(W_2N)_{1-x}C_x$ films using Atomic Force Microscopy (AFM). (f) Surface morphology at x = 0 and 0.25 of $(W_2N)_{1-x}C_x$ films.

sharply decreased since $W_2N$ phase is forced to be re–nucleated by segregation of C or $CN_x$ [29]. Fig. 2b–d present representative cross–sectional TEM images, HRTEM images, and selected area electron diffraction (SAED) patterns at x = 0, 0.11, and 0.25. Cross–sectional TEM image at x = 0 (Fig. 2a) exhibited rough surface with columnar porous structure film owing to the self–shadowing effect induced by sputtered particles [32]. The HRTEM image on the right–hand side shows fringe patterns with a d–spacing of 0.245 nm for (111) β–$W_2N$ planes. The SAED pattern contained corresponding (111), (200), (220), (311), (331), and (422) fcc β–$W_2N$ diffraction rings, which was in a good

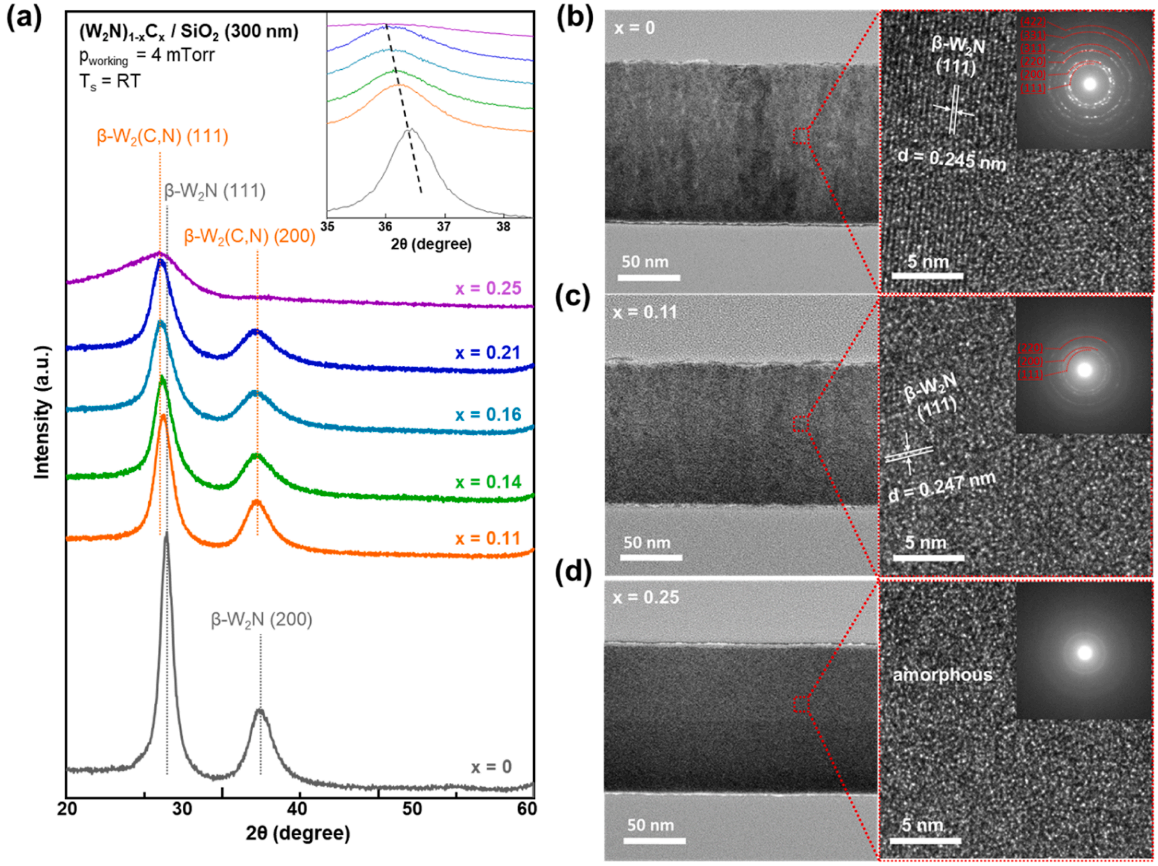


**Fig. 2.** (a) X–ray diffraction (XRD) patterns of $(W_2N)_{1\text{-}x}C_x$ films, (b–d) cross–sectional transmission electron microscopy (TEM) image, high resolution TEM (HRTEM), and selected area diffraction (SAED) patterns of $(W_2N)_{1\text{-}x}C_x$ films at x = 0, 0.11, and 0.25.

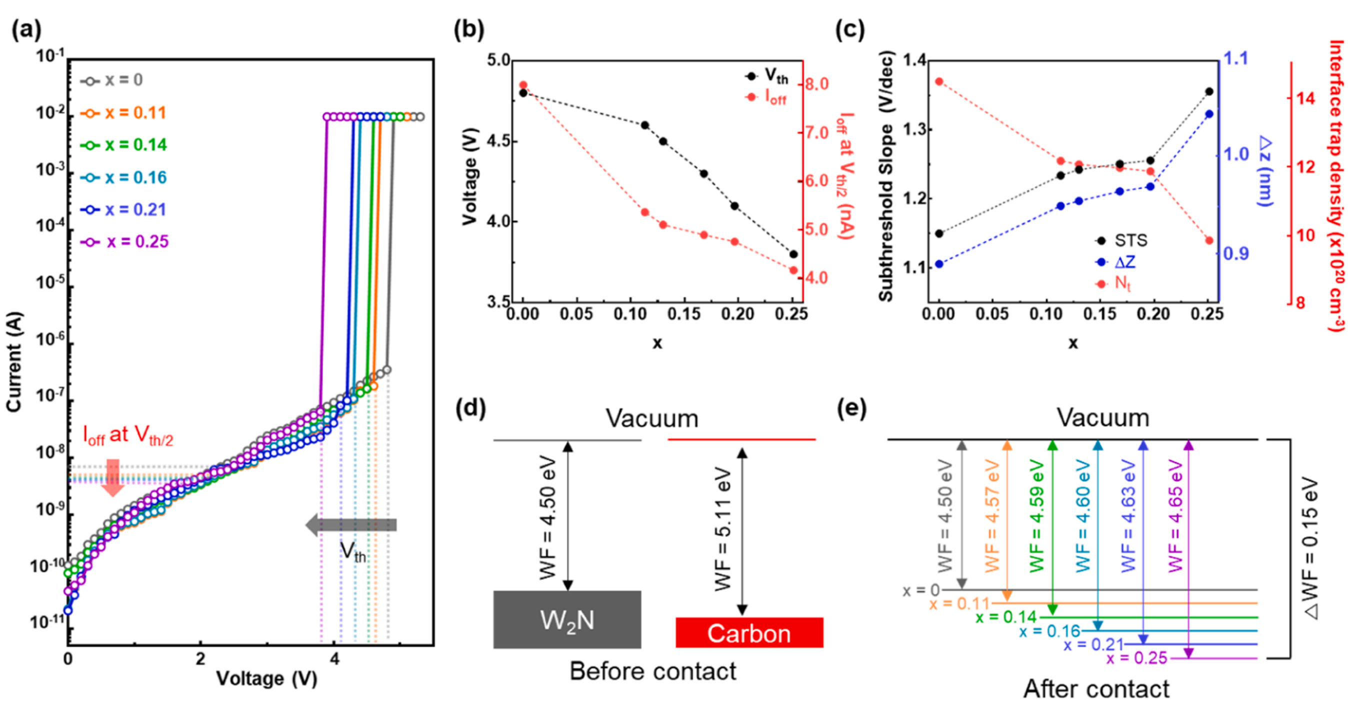


**Fig. 3.** (a) Electrical characteristics of $GeS_2$–based OTS selector device using $(W_2N)_{1\text{-}x}C_x$ ($0 \leq x \leq 0.25$) electrodes. (b) Comparison of threshold voltage ($V_{th}$) and off current ($I_{off}$) depend on $(W_2N)_{1\text{-}x}C_x$ electrodes. (c) Subthreshold slope (*STS*), distance between traps (*Δz*), and interface trap density ($N_{it}$), where values were extracted from measured I–V curve and PF–model. (d) Work function (WF) of $W_2N$ and amorphous carbon (a–C) before contact. (e) Calculated WFs of $(W_2N)_{1\text{-}x}C_x$ electrodes after ohmic contact between $W_2N$ and a–C.

agreement with JCPDS and other works. Fig. 2c shows TEM images with low C content (x = 0.11). Once C was incorporated, the film structure changed from continuous to discontinuous columnar. Note that the fringe patterns and amorphous matrix are mixed as shown in right–hand side HRTEM. The d–spacing increased to 0.247 nm with x = 0.11, which is well–matched with the peak shift in the XRD data. Fig. 2d demonstrates that the columnar grains completely disappeared with an extremely flat surface in the films with high C content (x = 0.25). No sharp fringe patterns were observed in HRTEM. The intensity of halo diffraction patterns in SAED was distinctively reduced, which is in a good agreement with our measured XRD data (purple color in Fig. 2a).

### 3.3. Electrical characteristics

The electrical characteristics of the $GeS_2$–based OTS selector device using $(W_2N)_{1-x}C_x$ ($0 \leq x \leq 0.25$) electrodes were measured under a voltage sweep of 0.1 V and a compliance current of 10 mA. The device was fabricated using DC and RF magnetron sputtering with a $(W_2N)_{1-x}C_x/GeS_2/W_2N$ structure, as shown in Figure S3a. Each layer plays role of top electrode, OTS selector, and bottom electrode with thicknesses of 100, 15, and 30 nm, respectively. A higher voltage than $V_{th}$ was applied to initiate the device. This process allows the device to obtain OTS behavior, which is called the "Firing process". The firing voltages ($V_{firing}$) were measured to be 6.5, 6.1, 5.8, 5.5, 5.4, and 5.1 V, respectively with increasing x as shown in Figure S3b. Fig. 3a demonstrates the I–V curves of $GeS_2$–based OTS devices based on different x contents. As x increased, both $V_{th}$ and $I_{off}$ decreased, reducing power consumption. Fig. 3b shows the $V_{th}$ and $I_{off}$ of $GeS_2$–based OTS devices using $(W_2N)_{1-x}C_x$ ($0 \leq x \leq 0.25$) electrodes. The $V_{th}$ was determined to be 4.8, 4.6, 4.5, 4.3, 4.1, and 3.8 V, respectively as the x in $(W_2N)_{1-x}C_x$ electrodes increased. Similarly, $I_{off}$ was measured to be 8.00, 5.37, 5.11, 4.90, 4.67, and 4.17 nA with increasing x. To classify the decreasing $V_{th}$ phenomenon, *STS* and inter–trap distance ($\Delta z$) were extracted using

$$\mathrm{STS} = \frac{\partial \log I}{\partial V_A} = \frac{q}{kT}\frac{\Delta z}{2U_a}$$

where $V_A$ denotes applied voltage, $q$ represents elementary charge, $k$ is Boltzmann constant, $T$ represents temperature, and $U_a$ is the thickness of the amorphous film [33]. From the above equation, *STS* can be calculated from the measured I–V curves with a $V_{th}$ range of 0.3 – 0.7 V. Fig. 3c shows *STS*, $\Delta z$, and $N_{it}$. The *STS* and $\Delta z$ increased from 1.15 to

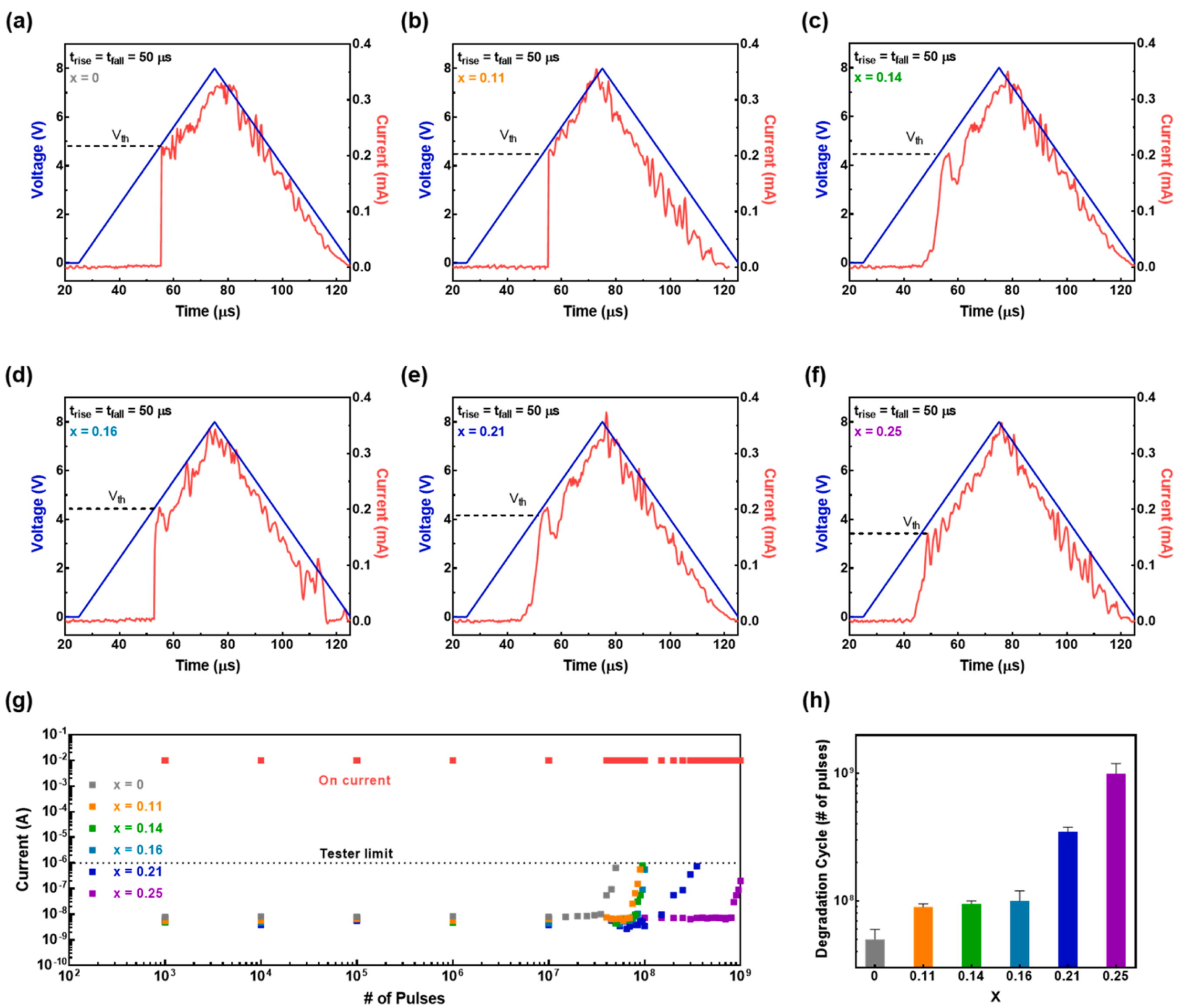


**Fig. 4.** Transient characteristics of $GeS_2$–based OTS selector device using $(W_2N)_{1-x}C_x$ ($0 \leq x \leq 0.25$) electrodes under triangular pulse height of 8 V with rising/falling time of 50 µs (a–f). (g) On and off currents after repeated pulses until currents increased up to tester limit. (h) Overall degradation cycle depend on contents of a–C.

1.35 V/dec and 0.890–1.045 nm, respectively. As $N_{it}$ is inversely proportional to $\Delta z^3$, the estimated $N_{it}$ decreased from $1.37 \times 10^{20}$ to $1.14 \times 10^{20}$ $cm^{-3}$. Decreased $N_{it}$ can be attributed to the decreasing roughness of $(W_2N)_{1\text{-}x}C_x$ with increasing x. The low roughness of the electrode is expected to reduce interfacial defects, which are composed of vacancies, dislocations, and grain boundaries [34]. Therefore, it minimizes charge trapping and allows charges to transport easily from the electrode to an insulating layer. The decrease in $V_{th}$ can be attributed to the decrease in $N_{it}$. Fig. 3d–e demonstrates WF of DC magnetron co–sputtered $(W_2N)_{1\text{-}x}C_x$ electrodes. The WFs were calculated to be 4.50 and 5.11 eV for $W_2N$ and a–C, respectively as shown in Fig. 3d [35,36]. As a–C was incorporated into $W_2N$, the pairs formed a metal–nonmetal Ohmic contact. Then, WF increased from 4.50 eV to 4.65 eV with increasing x to 0.25 as shown in Fig. 3e. Considering the p–type conductivity of the $GeS_2$ film, a high WF helps reduce the barrier height for hole injection as shown in Figures S3c–d schematic [25]. Therefore, increased WF allows holes to transport more easily from the electrode to the insulating layer, resulting in lower $V_{th}$. We believe that decreased $N_{it}$ and increased WF of $(W_2N)_{1\text{-}x}C_x$ electrodes attributed to a decrease in $V_{th}$.

### 3.4. Transient response and endurance

Fig. 4 demonstrates the transient characteristics of the $GeS_2$–based OTS selector device employing $(W_2N)_{1\text{-}x}C_x$ ($0 \leq x \leq 0.25$) electrodes. To prevent current overflow, a 10 kΩ load resistor was connected in series with a compliance current of 10 mA. Fig. 4a–f show the transient response of the $GeS_2$–based OTS selector device using $(W_2N)_{1\text{-}x}C_x$ electrodes with increasing x. The height of the triangular pulse was set to 8 V with a rising/falling time of 50 µs. When $V_A$ is lower than $V_{th}$, devices remained highly resistive with low current. Once $V_A > V_{th}$, currents sharply increased, corresponding to $V_{th}$ of X, 4.3, 4.2, 4.1, 4.0, and 3.8 V for devices based on $(W_2N)_{1\text{-}x}C_x$ electrodes with increasing x. Fig. 4g illustrates the endurance of the $GeS_2$–based OTS selector device using $(W_2N)_{1\text{-}x}C_x$ electrodes. Repeated AC pulses were applied until $I_{off}$ increased up to tester limit to investigate the lifetime. After $5.0 \times 10^7$ pulses $I_{off}$ of device with $(W_2N)_{1\text{-}x}C_x$ electrode at x = 0 began to increase, indicating device degradation. After incorporating C into $(W_2N)_{1\text{-}x}C_x$ electrodes, the lifetime enhanced to $9.0 \times 10^7$, $9.5 \times 10^7$, $1.0 \times 10^8$, $3.5 \times 10^8$, and $1.0 \times 10^9$ pulses for x = 0.11, 0.14, 0.16, 0.21, and 0.25, respectively. This enhanced lifetime with increasing C contents can be attributed to the prevention of W diffusion into the OTS layer. When repeated pulses are applied, transition metals such as W and Ti interact or diffuse with the chalcogenide materials and crystallize, causing devices degradation [21]. However, once C is incorporated, small atomic size of C prevents metal diffusion, allowing to maintain stable state. The $(W_2N)_{1\text{-}x}C_x$ electrode with the highest C contents showed superior endurance among the $(W_2N)_{1\text{-}x}C_x$ electrodes owing to the most compact networks, effectively preventing diffusion or interactions.

## 4. Conclusion

We explored the effect of vaying a–C content in $(W_2N)_{1\text{-}x}C_x$ ($0 \leq x \leq 0.25$) electrodes and its impact on $GeS_2$–based OTS selectors. The microstructure, electrical characteristics, and device lifetime of $(W_2N)_{1\text{-}x}C_x$ ($0 \leq x \leq 0.25$) electrodes were investigated using the $GeS_2$ as the selector layer. The XRD and HRTEM analyses confirmed the phase transformation from polycrystalline to amorphous with increasing a–C. The decreased roughness and increased density can be attributed to the reduced grain size. In electrical characteristics, both $V_{th}$ and $I_{off}$ of $GeS_2$–based OTS devices using $(W_2N)_{1\text{-}x}C_x$ ($0 \leq x \leq 0.25$) electrodes decreased from 4.8 to 3.8 V and 8.0–4.17 nA with increasing x. The higher WF and lower $N_{it}$ with increasing x allowed for a reduction in $V_{th}$. The enhanced device lifetime up to $1.0 \times 10^9$ pulses for the highest a–C content in $(W_2N)_{1\text{-}x}C_x$ ($0 \leq x \leq 0.25$) electrodes showed superior performance than that of other studies. This novel electrode offers stable and excellent performance, providing insight for future 3D X–point memory arrays.

## CRediT authorship contribution statement

**Jinhan Lee:** Formal analysis, Data curation. **Myoungsub Kim:** Validation, Methodology, Formal analysis. **Hyungjun Kim:** Data curation. **Sanghyeon Lee:** Writing – review & editing, Writing – original draft, Validation, Resources, Methodology, Investigation, Formal analysis, Data curation, Conceptualization. **Hyun S. Kum:** Data curation. **Sungjoon Cho:** Data curation. **Seungmin Lee:** Formal analysis. **Chihyeong Won:** Resources, Data curation. **Chaebeen Kwon:** Writing – original draft, Validation. **Kukro Yoon:** Data curation. **Minkyu Lee:** Writing – review & editing, Writing – original draft, Validation, Resources, Methodology, Investigation, Formal analysis, Data curation, Conceptualization. **Taeyoon Lee:** Supervision, Project administration, Funding acquisition. **Hanjoo Lee:** Data curation. **Jongho Ji:** Resources, Data curation. **Seunggyu Na:** Formal analysis.

## Declaration of Competing Interest

The authors declare that they have no known competing financial interests or personal relationships that could have appeared to influence the work reported in this paper.

## Acknowledgements

This paper was result of the research project supported by SK hynix Inc.

## Appendix A. Supporting information

Supplementary data associated with this article can be found in the online version at doi:10.1016/j.jallcom.2024.177102.

## Data availability

No data was used for the research described in the article.

## References

[1] G.W. Burr, R.M. Shelby, A. Sebastian, S. Kim, S. Kim, S. Sidler, K. Virwani, M. Ishii, P. Narayanan, A. Fumarola, L.L. Sanches, I. Boybat, M. Le Gallo, K. Moon, J. Woo, H. Hwang, Y. Leblebici, Neuromorphic computing using non-volatile memory, Adv. Phys. X. 2 (2017) 89–124, https://doi.org/10.1080/23746149.2016.1259585.
[2] A. Lotnyk, M. Behrens, B. Rauschenbach, Phase change thin films for non-volatile memory applications, Nanoscale Adv. 1 (2019) 3836–3857, https://doi.org/10.1039/c9na00366e.
[3] D.S. Jeong, C.S. Hwang, Nonvolatile memory materials for neuromorphic intelligent machines, Adv. Mater. 30 (2018) 1–27, https://doi.org/10.1002/adma.201704729.
[4] S. Li, C. Xu, Q. Zou, J. Zhao, Y. Lu, Y. Xie, Pinatubo: a processing-in-memory architecture for bulk bitwise operations in emerging non-volatile memories, Proc. - Des. Autom. Conf. 05-09-June (2016), https://doi.org/10.1145/2897937.2898064.
[5] G.W. Burr, R.S. Shenoy, K. Virwani, P. Narayanan, A. Padilla, B. Kurdi, H. Hwang, Access devices for 3D crosspoint memory, J. Vac. Sci. Technol. B, Nanotechnol. Microelectron. Mater. Process. Meas. Phenom. 32 (2014) 040802, https://doi.org/10.1116/1.4889999.
[6] Y. Xie, Y. Zhao, Emerging memory technologies, IEEE Micro 39 (2019) 6–7, https://doi.org/10.1109/MM.2019.2892165.
[7] D. Kau, S. Tang, I.V. Karpov, R. Dodge, B. Klehn, J.A. Kalb, J. Strand, A. Diaz, N. Leung, J. Wu, S. Lee, T. Langtry, K.W. Chang, C. Papagianni, J. Lee, J. Hirst, S. Erra, E. Flores, N. Righos, H. Castro, G. Spadini, A stackable cross point phase change memory, Tech. Dig. - Int. Electron Devices Meet. Iedm. (2009) 617–620, https://doi.org/10.1109/IEDM.2009.5424263.
[8] S.R. Ovshinsky, Reversible electrical switching phenomena in disordered structures, Phys. Rev. Lett. 21 (1968) 1450–1453, https://doi.org/10.1103/PhysRevLett.21.1450.
[9] D. Seong, S.Y. Lee, H.K. Seo, J.W. Kim, M. Park, M.K. Yang, Highly reliable ovonic threshold switch with TiN/GeTe/TiN structure, Materials 16 (2023) 1–9, https://doi.org/10.3390/ma16052066.
[10] W. Kim, C. Yoo, E.S. Park, M. Ha, J.W. Jeon, G.S. Kim, K.S. Woo, Y.K. Lee, C. S. Hwang, Electroforming-free bipolar resistive switching in GeSe thin films with a

Ti-containing electrode, ACS Appl. Mater. Interfaces 11 (2019) 38910–38920, https://doi.org/10.1021/acsami.9b10891.
[11] C.S. Kang, H.J. Cho, Y.H. Kim, R. Choi, C.Y. Kang, A. Shahriar, C.H. Choi, S.J. Rhee, J.C. Lee, Characterization of resistivity and work function of sputtered-TaN film for gate electrode applications, Proc. - Electrochem. Soc. 22 (2003) 215–220, https://doi.org/10.1116/1.1603285.
[12] R. Prakash, B.P. Singh Rathore, D. Kaur, Effect of top electrode material on resistive switching properties of WN based thin films for non volatile memory application, J. Alloy. Compd. 726 (2017) 693–697, https://doi.org/10.1016/j.jallcom.2017.07.184.
[13] S.K. Achar, J. Schneider, D.A. Stewart, Using machine learning potentials to explore interdiffusion at metal−chalcogenide interfaces, ACS Appl. Mater. Interfaces 14 (2022) 56963–56974, https://doi.org/10.1021/ACSAMI.2C16254.
[14] Y. Ding, J. An, J. Shen, S. Jia, J. Guo, L. Wang, T. Gong, P. Jiang, Y. Wang, Y. Chen, M. Zhu, C. Dou, Q. Luo, Low-voltage and high thermal stability single-element Te selector with failed bit pruning operation enabling robust cross-point memory, Adv. Electron. Mater. 8 (2022), https://doi.org/10.1002/aelm.202200870.
[15] G. Greczynski, D. Primetzhofer, J. Lu, L. Hultman, Core-level spectra and binding energies of transition metal nitrides by non-destructive x-ray photoelectron spectroscopy through capping layers, Appl. Surf. Sci. 396 (2017) 347–358, https://doi.org/10.1016/j.apsusc.2016.10.152.
[16] Z. Lin, S.R. Denny, J.G. Chen, Transition metal carbides and nitrides as catalysts for thermochemical reactions, J. Catal. 404 (2021) 929–942, https://doi.org/10.1016/j.jcat.2021.06.022.
[17] D.D. Kumar, N. Kumar, S. Kalaiselvam, S. Dash, R. Jayavel, Wear resistant super-hard multilayer transition metal-nitride coatings, Surf. Interfaces 7 (2017) 74–82, https://doi.org/10.1016/j.surfin.2017.03.001.
[18] I.S. Kim, C.E. Shim, S.W. Kim, C.S. Lee, J. Kwon, K.E. Byun, U. Jeong, Amorphous carbon films for electronic applications, Adv. Mater. 35 (2023) 1–21, https://doi.org/10.1002/adma.202204912.
[19] R.L. McCreery, Advanced carbon electrode materials for molecular electrochemistry, Chem. Rev. 108 (2008) 2646–2687, https://doi.org/10.1021/cr068076m.
[20] Y.V. Pleskov, Y.E. Evstefeeva, M.D. Krotova, V.V. Elkin, A.M. Baranov, A.P. Dement'Ev, Electrochemical behavior of amorphous carbon films: kinetic and impedance-spectroscopy studies, Diam. Relat. Mater. 8 (1999) 64–72, https://doi.org/10.1016/S0925-9635(98)00367-7.
[21] A. Verdy, G. Navarro, M. Bernard, S. Chevalliez, N. Castellani, E. Nolot, J. Garrione, P. Noe, G. Bourgeois, V. Sousa, M.C. Cyrille, E. Nowak, Carbon electrode for Ge-Se-Sb based OTS selector for ultra low leakage current and outstanding endurance, 6D.41-6D.46, IEEE Int. Reliab. Phys. Symp. Proc. 2018-March (2018), https://doi.org/10.1109/IRPS.2018.8353635.
[22] J.J. Hauser, Electrical, structural and optical properties of amorphous carbon, J. Non Cryst. Solids 23 (1977) 21–41, https://doi.org/10.1016/0022-3093(77)90035-7.
[23] A.V. Kolobov, J. Tominaga, P. Fons, T. Uruga, Local structure of crystallized GeTe films, Appl. Phys. Lett. 82 (2003) 382–384, https://doi.org/10.1063/1.1539926.
[24] S.D. Kim, H.W. Ahn, S.Y. Shin, D.S. Jeong, S.H. Son, H. Lee, B.K. Cheong, D. W. Shin, S. Lee, Effect of Ge concentration in GeXse1-x chalcogenide glass on the electronic structures and the characteristics of ovonic threshold switching (OTS) devices, ECS Solid State Lett. 2 (2013) 75–77, https://doi.org/10.1149/2.001310ssl.
[25] S. Jia, H. Li, T. Gotoh, C. Longeaud, B. Zhang, J. Lyu, S. Lv, M. Zhu, Z. Song, Q. Liu, J. Robertson, M. Liu, Ultrahigh drive current and large selectivity in GeS selector, Nat. Commun. 11 (2020) 1–9, https://doi.org/10.1038/s41467-020-18382-z.
[26] S.W. Yeh, T.T. Huang, J.W. Liu, S.H. Yu, C.H. Shih, J.K. Hwang, J. Echave, Local packing density is the main structural determinant of the rate of protein sequence evolution at site level, Biomed. Res. Int. 2014 (2014), https://doi.org/10.1155/2014/572409.
[27] H. Zhao, Z. Ni, F. Ye, Effect of carbon content on structure and properties of WCN coatings prepared by RF magnetron sputtering, Surf. Coat. Technol. 287 (2016) 129–137, https://doi.org/10.1016/j.surfcoat.2016.01.003.
[28] R. Ospina, D. Escobar-Rincón, P.J. Arango, E. Restrepo-Parra, J.F. Jurado, Structural and chemical composition analysis of WCN produced by pulsed vacuum arc discharge, Surf. Coat. Technol. 232 (2013) 96–100, https://doi.org/10.1016/j.surfcoat.2013.04.058.
[29] Y.D. Su, C.Q. Hu, M. Wen, C. Wang, D.S. Liu, W.T. Zheng, Effects of bias voltage and annealing on the structure and mechanical properties of WC0.75N0.25 thin films, J. Alloy. Compd. 486 (2009) 357–364, https://doi.org/10.1016/j.jallcom.2009.06.147.
[30] L. Yu, H. Zhao, J. Xu, Influence of silver content on structure, mechanical and tribological properties of WCN-Ag films, Mater. Charact. 114 (2016) 136–145, https://doi.org/10.1016/j.matchar.2016.02.013.
[31] L. Yu, H. Zhao, J. Xu, Mechanical, tribological and corrosion performance of WBN composite films deposited by reactive magnetron sputtering, Appl. Surf. Sci. 315 (2014) 380–386, https://doi.org/10.1016/j.apsusc.2014.07.170.
[32] M.L. Addonizio, A. Castaldo, A. Antonaia, E. Gambale, L. Iemmo, Influence of process parameters on properties of reactively sputtered tungsten nitride thin films, J. Vac. Sci. Technol. A Vac., Surf., Film. 30 (2012) 031506, https://doi.org/10.1116/1.3698399.
[33] J.A. Phys, Analytical model for subthreshold conduction and threshold switching in chalcogenide-based memory devices, 054517 (2010). https://doi.org/10.1063/1.2773688.
[34] I.J. Beyerlein, M.J. Demkowicz, A. Misra, B.P. Uberuaga, Defect-interface interactions, Prog. Mater. Sci. 74 (2015) 125–210, https://doi.org/10.1016/j.pmatsci.2015.02.001.
[35] P.C. Jiang, Y.S. Lai, J.S. Chen, Dependence of crystal structure and work function of WNX films on the nitrogen content, Appl. Phys. Lett. 89 (2006), https://doi.org/10.1063/1.2349313.
[36] A.V. Kesavan, B.R. Lee, K.R. Son, A.C. Khot, T.D. Dongale, V. Murugadoss, P. C. Ramamurthy, T.G. Kim, Work function-tunable amorphous carbon-silver nanocomposite hybrid electrode for optoelectronic applications, ACS Appl. Mater. Interfaces 13 (2021) 4284–4293, https://doi.org/10.1021/acsami.0c13937.